Article

An Arrhenius-Based Simulation Tool for Predicting Aging of Lithium Manganese Dioxide Primary Batteries in Implantable Medical Devices

Mahsa Doosthosseini *, Mahdi Khajeh Talkhoncheh, Jeffrey L. Silberberg and Hamed Ghods

Center of Device and Radiological Health (CDRH) at FDA, Office of Science and Engineering Laboratories (OSEL), Division of Biomedical Physics (DBP), White Oak Campus, Silver Spring, MD 20904, USA
* Correspondence: mahsa.doosthosseini@fda.hhs.gov

Abstract: This article presents a novel aging-coupled predictive thermo-electrical dynamic modeling tool tailored for primary lithium manganese dioxide (Li-MnO_2) batteries in active implantable medical devices (AIMDs). The aging mechanisms of rechargeable lithium batteries are well documented using computationally intensive physics-based models, unsuitable for real-time onboard monitoring in AIMDs due to their high demands. There is a critical need for efficient, less demanding modeling tools for accurate battery health monitoring and end-of-life prediction as well as battery safety assessment in these devices. The presented model in this article simulates the battery terminal voltage, remaining capacity, temperature, and aging during active discharge, making it suitable for real-time health monitoring and end-of-life prediction. We incorporate a first-order dynamic for internal resistance growth, influenced by time, temperature, discharge depth, and load current. By adopting Arrhenius-type kinetics and polynomial relationships, this model effectively simulates the combined impact of these variables on battery aging under diverse operational conditions. The simulation handles both the continuous micro-ampere-level demands necessary for device housekeeping and periodic high-rate pulses needed for therapeutic functions, at a constant ambient temperature of 37 °C, mimicking human body conditions. Our findings reveal a gradual, nonlinear increase in internal resistance as the battery ages, rising by an order of magnitude over a period of 5 years. Sensitivity analysis shows that as the battery ages and load current increases, the terminal voltage becomes increasingly sensitive to internal resistance. Specifically, at defibrillation events, the $\frac{\partial V}{\partial R}$ trajectory dramatically increases from 10^{-12} to 10^{-8}, indicating a fourth-order-of-magnitude enhancement in sensitivity. A model verification against experimental data shows an R² value of 0.9506, indicating a high level of accuracy in predicting the Li-MnO_2 cell terminal voltage. This modeling tool offers a comprehensive framework for effectively monitoring and optimizing battery life in AIMDs, therefore enhancing patient safety.

Keywords: primary Li-MnO_2 battery; aging-coupled thermo-electrical battery model; internal resistance growth; active implantable medical devices

1. Introduction

This article explores a simulation analysis focused on the discharge dynamics and aging behavior of lithium manganese dioxide (Li-MnO_2) primary batteries within active implantable medical devices (AIMDs). Studying the characteristics of primary lithium batteries in AIMDs is crucial, as the longevity of these implantable medical devices is tied solely to the longevity of their primary lithium battery power source. Given that battery replacement involves surgery to explant and replace the AIMD, ensuring the longevity of these cells is crucial for patient safety. This helps patients avoid surgical risks, emphasizing the need for the design of durable battery systems.

Table 1 presents a comprehensive summary of the various primary battery types used in cardiovascular implantable medical devices. Variability in capacity, operating

voltage, and energy density across the different battery types indicates that the choice of battery for an AIMD is tailored to the specific energy and voltage requirements of the device. Among these chemistries, $Li\text{-}MnO_2$ batteries have become prevalent due to their high-power output over brief periods. The construction of these batteries, whether coiled or stacked, enhances the electrode surface area, optimizing power capacity. A stable operating voltage of approximately 3 V is maintained through the initial discharge phase, providing a predictable measure for clinicians to gauge battery life. These features, along with their high power and consistent discharge behavior, render $Li\text{-}MnO_2$ cells a preferred choice for various implantable devices across multiple manufacturers [1–3].

**Table 1.** Batteries used in cardiovascular implantable medical devices [2].

Battery Type	Capacity (Ah)	Operating Voltage (V)	Longevity (year)	Energy Density (Wh/Kg)
$Li\text{-}I_2$	2.0–3.5	2.8	>10	210–270
$Li\text{-}MnO_2$	1.0–2.0	2.9	>10	230–270
$Li\text{-}CFx$	2	3.0	5–10	440
$Li\text{-}SVO$	0.9–2.0	2.4–2.8	5–10	270
$Li\text{-}MnO_2$	1.7–2.0	3.0	5–10	400

Primary $Li\text{-}MnO_2$ batteries used in implantable medical devices are subject to a distinctive set of challenges. They function continuously at approximately human body temperature, which is a steady 37 °C. This thermal environment precipitates the expedited aging of the battery. Moreover, these devices may not be actively used for extended periods, necessitating that the cells withstand long-term storage at both high and low states of charge, as well as under potential high-demand discharge conditions [4]. The application and environment of these cells introduce factors that accelerate aging. In AIMDs, constant exposure to body temperature accelerates chemical reactions; also, the high-power demands during the delivery of therapy affect the battery electrochemical reactions and initiate side reactions, leading to battery aging. Aging in lithium batteries in general occurs due to a combination of electrochemical reactions and physical changes within the cell over time, such as the gradual decomposition of electrolytes and the depletion of active materials [5]. Modeling aging mechanisms under various load conditions allows for precise end-of-life predictions, which is vital for scheduling battery replacements in a timely manner, thus preventing premature battery failure in critical medical devices. Battery aging is intrinsically linked to the growth of internal resistance; as the cell ages, chemical and physical transformations lead to increased resistance within the battery. This rise in resistance can manifest as a loss of available power, reduced efficiency, and eventual failure to meet the energy and power requirements of AIMDs [6]. Monitoring the internal resistance growth is therefore crucial for providing insights into the state of health of the battery and the remaining useful life of the cell. Accurately modeling this growth is essential for predicting when the battery will no longer perform optimally. The complexities of aging in $Li\text{-}MnO_2$ primary cells highlight the importance of modeling internal resistance increase, which acts as a reliable metric for battery degradation and is critical for assessing the operational lifespan of AIMDs [7]. While the aging mechanisms of rechargeable lithium batteries are extensively studied in the context of electric vehicles and energy storage systems [5,8,9], there is a lack of research focused on the modeling dynamics and aging of primary cells, including $Li\text{-}MnO_2$ chemistries for AIMD applications. To the best of the authors' knowledge, this represents a significant gap in the literature, underscoring the importance of developing comprehensive models to predict and mitigate the effects of aging in these vital devices. Despite considerable progress in modeling and incorporating $Li\text{-}MnO_2$ batteries in implantable cardioverter defibrillators (ICDs), certain challenges persist, as evidenced by prior research, including the study conducted by Manolis et al. [10].

While manufacturers typically assure 7- to 11-year projected longevity for ICDs [11], real-world data reveal that not all devices achieve this promised lifespan [12]. Remarkably, approximately 8% of ICDs experienced premature battery depletion within a mere 3-year period in a population-based study of 685 patients [13]. To address this critical issue, we propose a comprehensive simulation model that utilizes an aging-coupled thermo-electrical dynamic model for primary lithium batteries in ICDs. In Section 2, we explore the voltage characteristics and depth of discharge (DOD) behavior of the Li-MnO_2 battery. We also conduct an experiment to illustrate primary battery aging through its internal resistance growth. Section 3 describes the Li-MnO_2 aging-coupled thermo-electrical model. Further, Section 4 presents the simulation results for an average ICD load including defibrillation, and device supply currents, allowing us to gain valuable insights into battery dynamics and lifespan. Furthermore, in this section, we present the model verification results by comparing the battery terminal voltage predictions with the experimental data obtained from our laboratory. We also perform a sensitivity analysis on the battery initial internal resistance estimation to investigate the feasibility of using this model for aging prediction. Finally, we summarize our findings in Section 5.

2. Li-MnO_2 Battery Discharge Characteristics

In Li-MnO_2 batteries, the cathode is composed of manganese dioxide (MnO_2), and the anode is made from lithium (Li). During the battery's discharge cycle, lithium at the anode oxidizes to release Li ions, which then travel through the electrolyte to the cathode. Here, they engage in a reaction, likely involving the insertion of lithium ions into the hexagonal close-packed oxygen lattice of the MnO_2 material as shown in Equation (1). This intercalation process modifies the MnO_2 structure, underpinning the multi-step discharge process of these cells [14]:

$$xLi + MnO_2 \longrightarrow Li_xMnO_2 \ \ (0 \leq x \leq 0.1) \tag{1}$$
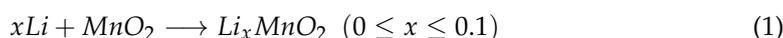
The discharge characteristics of Li-MnO_2 cells are significantly influenced by the structural and compositional features of the MnO_2 which yield three distinct stages in the discharge profile, each indicative of structural evolution within the MnO_2. We discharged a fresh Panasonic CR2450 Li-MnO_2 primary cell with a capacity of 620 mAh at a constant current of 1 mA using an Arbin LBT20084 (College Station, TX, USA) battery testing system. This low discharge current is crucial, as it ensures that the battery's terminal voltage closely approximates its open circuit voltage, minimizing the impact of internal resistance on the voltage reading. Over the course of 537.31 h, the voltage of the cell decreased from 3.3 V to 0.3 V. To generate the DOD-OCV curve, the discharged current was integrated over time to calculate the depth of discharge based on the coulomb counting method as shown in Equation (2), which is a measure of how much of the battery's capacity has been used. In this equation, Q is the battery nominal capacity, t is time, and I is the discharge current in amperes. The resulting DOD-OCV characteristic curve (Figure 1) shows how the voltage decreases as the battery is progressively discharged. This curve is essential for understanding the operational performance of the battery, particularly for applications where predicting the remaining useful life and usable capacity of the cells is critical:

$$DOD(\%) = 1 - 1/Q \int I(t)dt, \tag{2}$$

According to Figure 1, initially, within the first 10% of discharge, there is a homogeneous reaction, where lithium ions integrate into the MnO_2 lattice to form Li_xMnO_2, with x values less than 0.1 in Equation (1). This phase of the reaction is revealed by the sloping segments of the discharge and recovery curves. The subsequent stage, occurring between about 10% and 40% depth of discharge, corresponds with a heterogeneous or two-phase reaction. This is characterized by a plateau in the voltage curve, which signifies a phase transition in the cathode material. The concluding discharge phase reverts to a

homogeneous reaction, suggesting the further insertion of lithium ions into a new structural form of $Li_x MnO_2$, where x is greater than 0.4. This last stage underscores the complexity and dynamic nature of the electrochemical reactions in $Li\text{-}MnO_2$ batteries, integral to their functionality in demanding applications such as AIMDs. The experiment to obtain the Figure 1 curve for the $Li\text{-}MnO_2$ cell was conducted to integrate this curve into the battery model, as the terminal voltage of the battery is a function of both the battery characteristic DOD-OCV relationship and the voltage drops across equivalent circuit components of the model detailed in the next section.
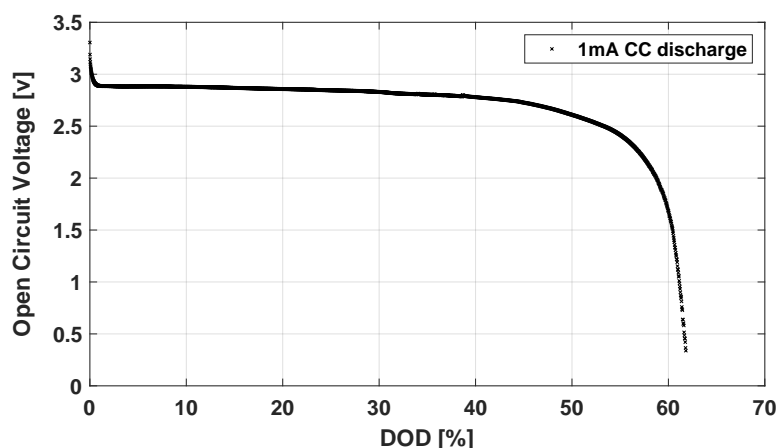

Figure 1. OCV-DOC curve for a fresh 620 mAh CR2450 $Li\text{-}MnO_2$ battery which is discharged with 1 mA constant current.

Another experiment was (Figure 2) conducted to empirically demonstrate aging in primary $Li\text{-}MnO_2$ batteries, specifically through increased internal resistance. A 90 mA discharge current at a constant ambient temperature of 37 °C was applied to two CR2450 primary $Li\text{-}MnO_2$ cells with 620 mAh initial capacity. One of them was a fresh cell, the other one was an aged cell. Both cells had similar initial open circuit voltages at 3.3 V and they underwent a discharge process until the battery terminal voltages decreased to the 1.5 V cut-off voltage. The aged cell was aged by being heated constantly in a thermal chamber at 55 °C for two weeks. By considering an Arrhenius-type growth rate for the internal resistance dynamics, the experiment showed thermally accelerated aging in the aged cell compared to the fresh cell.

The accelerated aging of the second $Li\text{-}MnO_2$ cell, achieved by subjecting it to a high temperature, for example at 55 °C for two weeks, is a practical application of the Arrhenius equation's principle that higher temperatures expedite chemical reactions, thereby simulating an expedited aging process. This method offers a predictive model for the cell's long-term behavior at lower operational temperatures, like 37 °C. The fresh cell sustained a higher voltage over an extended duration relative to its aged counterpart, implying an increase in the internal resistance in the aged cell due to the accelerated aging. This increase typically manifests as a more pronounced voltage drop under load. Furthermore, the aged cell's discharge curve indicates a noticeable reduction in capacity, a characteristic consequence of aging in batteries where the efficiency of electrochemical energy conversion diminishes over time, especially under thermal stress. In summary, the aged cell demonstrates significant internal resistance increase and capacity decrease, with the initial voltage drops being markedly steeper (approximately 0.4 volts) compared to the fresh cell, underscoring the critical impact of aging on battery performance.
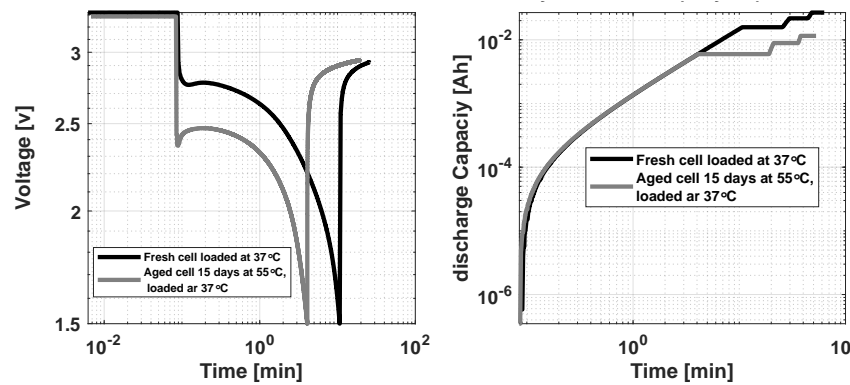
Figure 2. Fresh versus aged *Li-MnO₂* cells at 37 °C temperature under 90 mA discharge current followed by 15 min rest.

These data show that temperature, current magnitude, and depth of discharge significantly influence battery aging and degradation. In the subsequent section, we develop a model where the rate of change in internal resistance is functionally dependent on these parameters. Considering a first-order dynamics for internal resistance, we describe its variation over time, influenced by the battery discharge current, temperature, and depth of discharge.

3. *Li-MnO₂* Battery Arrhenius-Based Thermo-Electrical Dynamic Model

The model depicted in Figure 3 is structured as a lumped parameter equivalent circuit model (ECM) coupled with the battery internal temperature and resistance dynamics. This model was also studied for *Li-SVOCFx* battery chemistry in ICD applications by [15]. The integrated aging dynamic is specifically added to the model to represent the cell's internal resistance growth. The model in Equation (3) encompasses key elements such as the discharge current (I), capacity (Q), polarization capacitance (C_1), polarization resistance (R_1), internal ohmic resistance (R_2), and ICD defibrillation capacitor (C_d). The model includes four state variables, $x_1(t)$, $x_2(t)$, $x_3(t)$ and $x_4(t)$, which represent the depth of discharge (DOD), the transient voltage, the internal temperature, and internal resistance of the battery. The thermal dynamics are addressed by connecting the nonlinear behavior of the lithium battery cell temperature (x_3) with the ECM model through Bernardi's temperature dynamics model [16]. This method has been employed in the literature for analyzing battery parameter identifiability and estimating parameters [17].
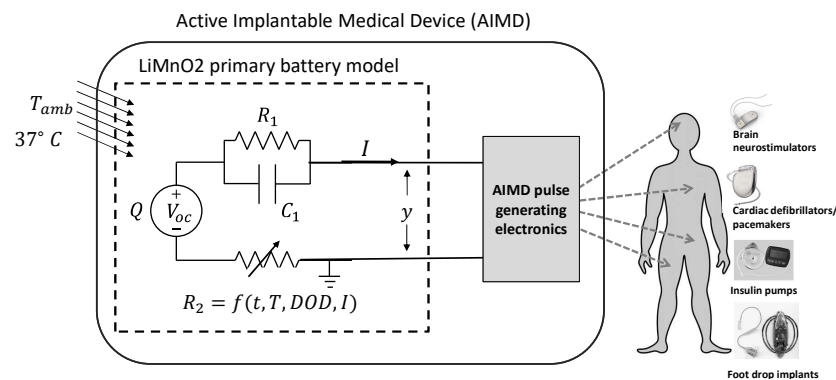

Figure 3. The aging-coupled thermo-electrical model of a lithium battery in an AIMD.

$$\dot{x}_1 = \frac{1}{Q}I$$

$$\dot{x}_2 = \frac{1}{R_1 C_1}x_2 + \frac{I}{C_1}$$

$$\dot{x}_3 = \frac{hA}{mC_p}(T_{amb} - x_3) + \frac{x_4}{mC_p}I^2 + \frac{\mu(x_2)}{mC_p}x_3 I \qquad (3)$$

$$\dot{x}_4 = K_{R_2}x_4$$

$$K_{R_2} = a_1 \times x_1^{a_2} + a_3 \times e^{\frac{-a_4}{x_3}} + a_5 \times I^{a_6}$$

$$y = OCV(x_1) + \frac{x_2}{C_1} + x_4 I$$

The x_3 dynamics capture three crucial phenomena. First, the term $mC_p\frac{dT}{dt}$ accounts for the battery cell's capacity to store thermal energy, where T is the cell temperature, m is the mass, and C_p is the specific heat capacity. Second, the term $hA(T_{amb} - x_3)$ describes the convective heat exchange between the battery and its environment, with h as the convective heat transfer coefficient, A as the convective area, and T_{amb} as the ambient temperature. By including T_{amb} as an input in the model, we can capture the influence of body temperature variations on the cell's internal temperature, allowing the model to account for thermal changes in different physiological conditions. Lastly, the term $R_2 I^2$ reflects the generation of heat due to resistance, with $x_4(t)$ representing the cell's ohmic resistance as a first-order variable. The internal resistance growth rate K_{R_2} incorporates a polynomial relationship with the battery depth of discharge, an exponential Arrhenius-type dependency on the battery temperature, and a polynomial correlation with the battery input current.

A similar approach was also studied in [18] for rechargeable $LiFePO_4$/graphite battery health-coupled modeling dynamics for states and parameter estimation in electric vehicle application. Specifically, the exponential ($a_3 \times e^{\frac{-a_4}{x_3}}$) in the rate constant function is essential for capturing the nonlinear impact of temperature on battery aging, consistent with Arrhenius' law where a_3 is analogous to the Arrhenius pre-exponential factor and a_4 represents the activation energy in the Arrhenius equation. This term reflects the accelerated aging at elevated temperatures and provides a theoretical basis for understanding temperature dependence in battery aging. The term ($a_1 \times x_1^{a_2}$) in the internal resistance growth rate addresses the nonlinear interplay between the battery's available charge and resistance. Moreover, the term ($a_5 \times I^{a_6}$) is used to capture the dependency of the internal resistance growth rate on the magnitude of the battery discharge current. The summation of these three aging components suggests variable aging rates contingent upon the battery's charge level, temperature, and discharge current, thereby providing a comprehensive and theoretically grounded framework for understanding and predicting battery aging dynamics. The final term in Equation (3) represents the battery terminal voltage (y), which serves as the output of the model. This voltage (y) consists of the cell's open circuit voltage as a function of the depth of discharge, the voltage drop across the $R_1 C_1$ pair, and the voltage drop due to the internal resistance (R_2). The nominal parameters for the model, relating to commercially available Li-MnO_2 battery cells with a similar ICD cell's capacity, are listed in Table 2, sourced from [19,20]. Moreover, the aging parameters were selected and adjusted to reflect an internal resistance growth of one order of magnitude for Li-MnO_2 battery used in implantable devices over their 100% depth of discharge based on the work conducted by Root [21]. The parameters in Table 2 are selected based on their relevance and validation in similar battery modeling contexts. However, no parameter optimization

has been conducted in this study to specifically enhance the model's accuracy against our experimental data.

In this study, we utilize the dynamic model to simulate the discharge behavior of an ICD battery over five years. This simulation aims to predict the aging and performance of the battery under conditions that include an average device housekeeping current of 25 μA and a typical current needed for charging the high-voltage capacitor for defibrillation pulse generation, which is assumed to be one defibrillation event per year. Each one of these defibrillation events is a series of three pulses with 10 s pulse-width and magnitude of 1 A. The open-circuit voltage (OCV) is a function of the depth of discharge (DOD), $OCV(x_1)$, which is a characteristic curve unique to each battery chemistry. For the *Li-MnO$_2$* battery, the OCV-DOD curve used in this model is experimentally obtained as detailed in Section 2.

The model presented in Equation (3) is Lipschitz continuous, ensuring the existence of a unique solution given the initial conditions. We solve this model using the Euler method, assuming the initial depth of discharge for the *Li-MnO$_2$* battery is 5% (indicating the battery is nearly fully charged with a 95% state of charge). Additionally, the battery's initial temperature is set to match the patient's core body temperature ($x_3(0) = 37°$), and the initial transient voltage is assumed to be zero. The results and corresponding discussion are provided in the following section.

Table 2. *Li-MnO$_2$* battery model parameters.

Parameter	Values, Unit	Parameter	Values, Unit
Q	620 [mAh]	h	11 [J/s·m^{2}K]
A	3×10^{-4} [m^2]	m	0.03 [kg]
I	25 [μA]	R_1	0.11 [Ω]
$R_2(0)$	0.27 [Ω]	C_1	2.35×10^3 [F]
a_1	1×10^{-9}	a_2	1
a_3	1.47×10^{-8}	a_4	5×10^{-5}
a_5	1×10^{-5}	a_6	5

4. Results

For the simulation study on this model, we choose to apply input current values analogous to the load of an ICD since these values are more readily available in the literature. The replacement time in ICDs is determined by a significant drop in the battery terminal voltage, occurring at approximately 2.5 V, or after the knee in the voltage curve [22,23]. A steady current of 25 μA for housekeeping and a defibrillation current of 1.0 A, with a pulse duration of 10 s and occurring once a year, are applied to the *Li-MnO$_2$* battery model. These parameters are sourced from the work performed by Root and Baliga [21,24]. The battery starts with an initial voltage of 3.3 V.

Figure 4 shows the simulation results for the terminal voltage and the battery depth of discharge. The voltage drop progressively becomes more pronounced for every defibrillation pulse sequence. The depth of discharge (DOD) plot in Figure 4 indicates a steady decline in battery capacity throughout the device's lifespan.

Figure 5 illustrates the internal temperature of the battery over the device's operational life. During normal operation for device housekeeping, the temperature remains close to 37 °C but begins to exceed 37.5 °C following each defibrillation after the third year. The thermal time constant, defined as $\frac{mC_p}{hA}$ in this model, is quite small (approximately 10^{-3}), leading to a rapid return of the temperature to its equilibrium state. This model effectively captures the dynamics of battery voltage and depth of discharge during typical usage in an ICD. It accurately predicts battery failure in the device by estimating when the battery voltage will drop below 2 V, at which point the battery will be unable to deliver the necessary energy.
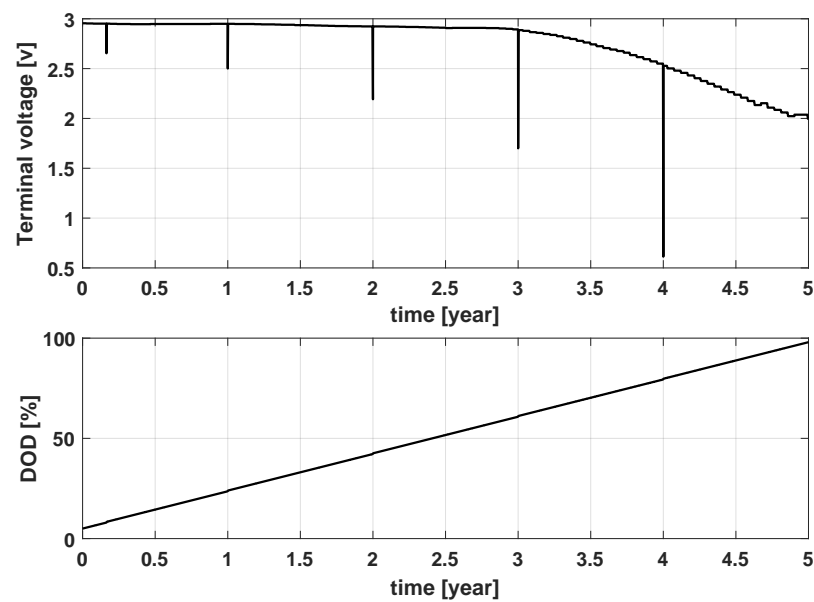
Figure 4. Terminal voltage and depth of discharge (DOD) of a primary *Li-MnO$_2$* battery with nominal 620 mAh capacity subjected to ICD housekeeping and defibrillation loads.
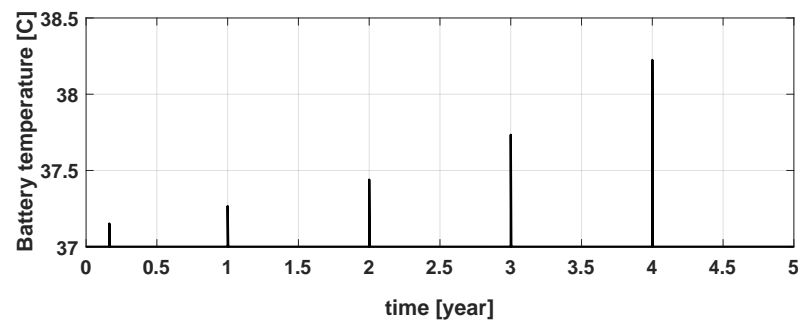

Figure 5. Internal temperature profile of the battery under ICD housekeeping and defibrillation load.

Figure 6 shows the battery internal resistance growth estimation due to battery aging in 5 years, as the battery provides an average load for an ICD. The internal resistance in the model has a first-order dynamic; however, its trajectory is not linear because of the inconstant and nonlinear nature of the internal resistance growth rate (K_{R_2}), which is a function of the battery temperature, load, and charge. The magnified portion of Figure 6 focuses on the fourth defibrillation event in year three. According to this simulation result, the battery internal resistance increase has a surge right at the time. This surge is almost 200 µohm. It suggests that defibrillation pulses degrade the battery faster. Therefore, estimating the battery internal resistance during the battery life in an AIMD is a gauge for predicting battery health and longevity. This model simulation does not account for external factors leading to battery failure, such as current leakage caused by ICD lead insulation issues or device malfunctions. Additionally, it does not consider internal battery failure mechanisms, including internal short circuits. However, the model can potentially be used in AIMD battery management systems to predict the battery voltage, depth of discharge, and internal resistance growth as aging mechanisms affecting battery health to more accurately predict battery and device end of life.
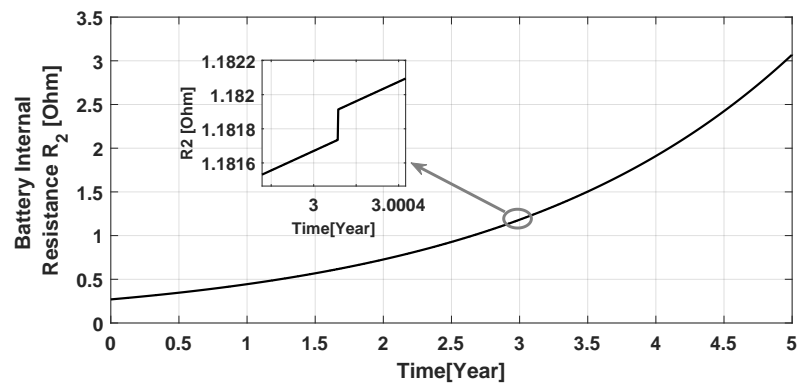
Figure 6. *Li-MnO$_2$* Internal resistance increases from 0.27 [Ω] to 3 [Ω] during 5 years of operation in an ICD.

We conducted an experiment to evaluate whether this model can accurately predict the discharge behavior of a *Li-MnO$_2$* coin cell under a load pattern mimicking that of an ICD. This pattern includes a continuous low-rate current for housekeeping functions and two-pulse high-rate currents simulating defibrillation. The results presented here are derived from a preliminary model with parameters that have not yet been optimized for the best fit to the experimental data. Figure 7 illustrates the comparison between the experimental discharge data of a CR2450 *Li-MnO$_2$* nonrechargeable cell and the predictions from the aging and thermally coupled equivalent circuit model presented in this article. The experiment, conducted at 37 °C with a combined load of 25 µA continuous and 15 mA discharge current pulses, demonstrates the model's ability to accurately replicate real-world battery behavior. Notably, the model captures the voltage drops and subsequent recoveries during the pulse discharges with high fidelity. The model's predictions align closely with the experimental data, indicating its robustness in simulating battery performance under dynamic load conditions. To quantify the model's accuracy, a goodness-of-fit analysis was performed, yielding a coefficient of determination (R^2) of 95.06%. This high value underscores the model's precision and reliability, affirming its utility for predicting battery behavior in practical applications.
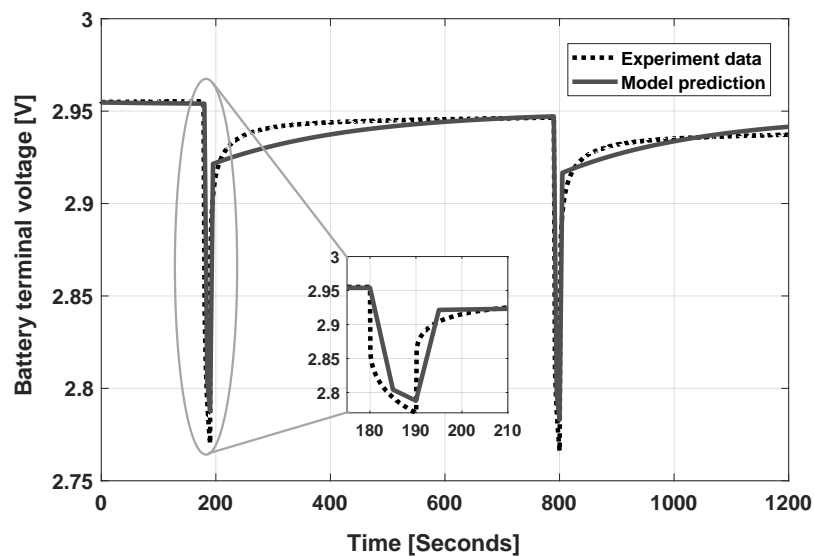

Figure 7. Prediction of the model for a fresh CR2450 *Li-MnO$_2$* nonrechargeable cell at 37 °C under a combined load of 25 µA continuous and 15 mA pulse discharge currents (experimental data are generated using the Arbin BLT20084 battery test machine).

Predicting battery aging by solving the battery internal resistance as a state in Equation (3) is feasible if we assume that the initial battery internal resistance is known or if we can estimate it from the battery measured output, which is the battery terminal voltage. Here, we conducted a sensitivity analysis on the battery's initial internal resistance to investigate the sensitivity of the battery terminal voltage to this parameter. Sensitivity analysis techniques are commonly employed to examine the practical identifiability of dynamic systems. The process typically starts by evaluating how sensitive the system's output is to changes in the underlying parameters. To perform sensitivity analysis, an output variable $Y(t, \theta)$ is defined, corresponding to the true open circuit voltage V at time t, for an unknown initial state θ. Although measurements of this output variable are subject to noise, $Y(t, \theta)$ represents the true output, unaffected by noise.

Assume that the output $Y(t, \theta)$ is recorded at intervals separated by a sampling time $\delta t = 5$ s. Further, assume that the measured output at each sampling instance equals the true value plus an independent and identically distributed noise signal with zero mean and a certain variance σ^2. Let $Y(k\delta t, \theta)$ denote the actual value of the output at time $t = k\delta t$, given a particular unknown parameter θ. The sensitivity function $s(k\delta t)$ is then defined as follows:

$$s(k\delta t) = \lim_{\delta\theta \to 0} \frac{Y(k\delta t, \theta + e_i \delta\theta) - Y(k\delta t, \theta)}{\delta\theta} \tag{4}$$

where $\delta\theta$ denotes a very small variation in the unknown parameter (θ is the initial battery internal resistance).

Figure 8 shows that as the *Li-MnO$_2$* battery ages, its terminal voltage becomes increasingly sensitive to variations in the battery internal resistance. Early in its lifespan, changes in resistance have a relatively minor impact on the voltage, but as time progresses, even small changes in the internal resistance can lead to more significant changes in the terminal voltage. Specifically, at defibrillation events, the $\frac{\partial V}{\partial R_2}$ trajectory dramatically increases from 10^{-12} to 10^{-8}, indicating a fourth-order-of-magnitude enhancement in sensitivity. This result implies that the battery's initial internal resistance becomes increasingly identifiable over time, particularly as the battery ages and the load intensifies. This trend indicates that our model could be utilized effectively to estimate the internal resistance as an aging mechanism for AIMDs.
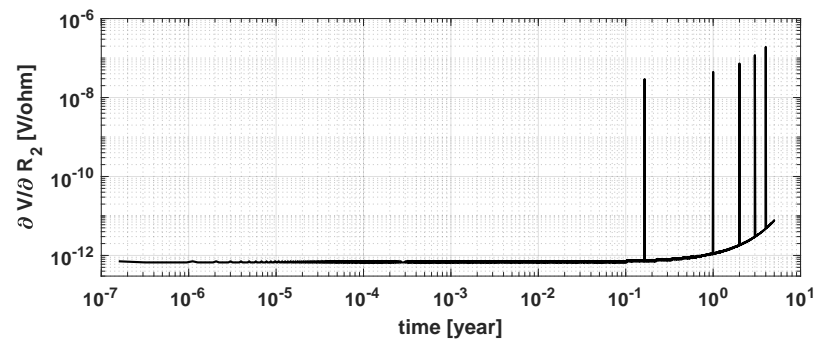

Figure 8. Sensitivity of the *Li-MnO$_2$* battery terminal voltage to the perturbation of the battery initial internal resistance under an average ICD load in 5 years.

5. Conclusions

This paper presents a simulation-based analysis of primary *Li-MnO$_2$* batteries in implantable medical devices, focusing on the depth of discharge, internal temperature, and internal resistance of the cell. The aging model incorporates dynamics influenced by time, temperature, discharge depth, and load current, with a constant 37 °C to simulate body conditions. It considers both low-power continuous operation and high-power pulses, using input currents akin to those of an ICD based on the literature data. Our simulations show a linear decrease in battery capacity and an increasing voltage drop magnitude and

temperature at each defibrillation event. Furthermore, the study highlights the internal resistance's growth due to aging in AIMDs, characterized by a nonlinear trajectory as a function of the temperature, load, and battery depth of discharge. Sensitivity analysis demonstrates that as the battery ages, its terminal voltage becomes increasingly sensitive to changes in the internal resistance, particularly during defibrillation events. The results suggest that the model can be used by AIMD battery management systems to estimate internal resistance as a key aging mechanism. Moreover, the precision in estimating age-related parameters can be enhanced by optimizing the load current to amplify the output's sensitivity to variations in the aging parameters, thereby ensuring more accurate aging predictions. This approach, however, does not account for external battery failure causes or internal battery failures like short circuits or thermal runaway. Despite these limitations, the simulation model can potentially be used for optimizing battery design in implantable medical devices to prolong battery life, thereby improving patient care.

References

1. Leong, A.M.; Arnold, A.D.; Whinnett, Z.I. Implantable Cardioverter Defibrillator Tachycardia Therapies: Past, Present and Future Directions. *J. Cardiovasc. Dev. Dis.* **2024**, *11*, 92. [CrossRef] [PubMed]
2. Deng, J.; Sun, X.; Peng, H. Power supplies for cardiovascular implantable electronic devices. *EcoMat* **2023**, *5*, e12343. [CrossRef]
3. Hauser, R.G.; Casey, S.A.; Gitter, C.B.; Tang, C.Y.; Abdelhadi, R.H.; Gornick, C.C.; Stanberry, L.; Sengupta, J.D. Reliability and longevity of implantable defibrillators. *J. Interv. Card. Electrophysiol.* **2021**, *62*, 507–518. [CrossRef] [PubMed]
4. Deer, T.R.; Pope, J.E.; Falowski, S.M.; Pilitsis, J.G.; Hunter, C.W.; Burton, A.W.; Connolly, A.T.; Verrills, P. Clinical longevity of 106,462 rechargeable and primary cell spinal cord stimulators: Real world study in the medicare population. *Neuromodul. Technol. Neural Interface* **2023**, *26*, 131–138. [CrossRef] [PubMed]
5. Han, X.; Lu, L.; Zheng, Y.; Feng, X.; Li, Z.; Li, J.; Ouyang, M. A review on the key issues of the lithium ion battery degradation among the whole life cycle. *ETransportation* **2019**, *1*, 100005. [CrossRef]
6. Cortner, J.M.; Dizon, E.; Rodriguez-Alvarez, J. Testing lifetime performance of primary batteries. *IEEE Instrum. Meas. Mag.* **2013**, *16*, 26–31. [CrossRef]
7. Harding, J.R.; Han, B.; Madden, S.B.; Horn, Q.C. Examining the performance of implantable-grade lithium-ion cells after overdischarge and thermally accelerated aging. *Energies* **2022**, *15*, 1405. [CrossRef]
8. Xiong, R.; Pan, Y.; Shen, W.; Li, H.; Sun, F. Lithium-ion battery aging mechanisms and diagnosis method for automotive applications: Recent advances and perspectives. *Renew. Sustain. Energy Rev.* **2020**, *131*, 110048. [CrossRef]
9. Edge, J.S.; O'Kane, S.; Prosser, R.; Kirkaldy, N.D.; Patel, A.N.; Hales, A.; Ghosh, A.; Ai, W.; Chen, J.; Yang, J.; et al. Lithium ion battery degradation: What you need to know. *Phys. Chem. Chem. Phys.* **2021**, *23*, 8200–8221. [CrossRef]
10. Manolis, A.S.; Maounis, T.; Koulouris, S.; Vassilikos, V. "Real life" longevity of implantable cardioverter-defibrillator devices. *Clin. Cardiol.* **2017**, *40*, 759–764. [CrossRef]
11. Knight, B.P.; Clementy, N.; Amin, A.; Birgersdotter-Green, U.M.; Roukoz, H.; Holbrook, R.; Manlucu, J. The clinical and economic impact of extended battery longevity of a substernal extravascular implantable cardioverter defibrillator. *J. Cardiovasc. Electrophysiol.* **2024**, *35*, 230–237. [CrossRef] [PubMed]

12. Lazzeri, M.; Ziacchi, M.; Angeletti, A.; Carecci, A.; Bertelli, M.; Locchi, F.; Oppimitti, J.; Biffi, M. Unanticipated subcutaneous ICD end-of-service due to premature battery depletion and occurrence of lead fracture: A single centre experience. *Int. J. Cardiol.* **2024**, *400*, 131687. [CrossRef] [PubMed]

13. Lüker, J.; Strik, M.; Andrade, J.G.; Raymond-Paquin, A.; Elrefai, M.H.; Roberts, P.R.; Pérez, Ó.C.; Kron, J.; Koneru, J.; Franqui-Rivera, H.; et al. Incidence of premature battery depletion in subcutaneous cardioverter-defibrillator patients: Insights from a multicenter registry. *J. Interv. Card. Electrophysiol.* **2023**. [CrossRef] [PubMed]

14. Shin, J.; Seo, J.K.; Yaylian, R.; Huang, A.; Meng, Y.S. A review on mechanistic understanding of MnO2 in aqueous electrolyte for electrical energy storage systems. *Int. Mater. Rev.* **2020**, *65*, 356–387. [CrossRef]

15. Doosthosseini, M.; Ghods, H.; Talkhoncheh, M.K.; Silberberg, J.L.; Weininger, S. Hybrid Cathode Lithium Battery Discharge Simulation for Implantable Cardioverter Defibrillators Using a Coupled Electro-Thermal Dynamic Model. *Cardiovasc. Eng. Technol.* **2023**, *14*, 534–543. [CrossRef]

16. Bernardi, D.; Pawlikowski, E.; Newman, J. A general energy balance for battery systems. *J. Electrochem. Soc.* **1985**, *132*, 5–12. [CrossRef]

17. Doosthosseini, M.; Fathy, H.K. On the Structure of the Optimal Input for Maximizing Lithium-Ion Battery Thermal Parameter Identifiability. In Proceedings of the 2020 American Control Conference (ACC), Denver, CO, USA, 1–3 July 2020 ; IEEE: New York, NY, USA, 2020; pp. 379–385.

18. Vennam, G.; Sahoo, A. A dynamic soh-coupled lithium-ion cell model for state and parameter estimation. *IEEE Trans. Energy Convers.* **2022**, *38*, 1186–1196. [CrossRef]

19. Gomadam, P.M.; Merritt, D.R.; Scott, E.R.; Schmidt, C.L.; Skarstad, P.M.; Weidner, J.W. Modeling lithium/hybrid-cathode batteries. *J. Power Sources* **2007**, *174*, 872–876. [CrossRef]

20. Manane, Y.; Yazami, R. Accurate state of charge assessment of lithium-manganese dioxide primary batteries. *J. Power Sources* **2017**, *359*, 422–426. [CrossRef]

21. Root, M.J. Lithium–manganese dioxide cells for implantable defibrillator devices—Discharge voltage models. *J. Power Sources* **2010**, *195*, 5089–5093. [CrossRef]

22. Chen, K.; Merritt, D.R.; Howard, W.G.; Schmidt, C.L.; Skarstad, P.M. Hybrid cathode lithium batteries for implantable medical applications. *J. Power Sources* **2006**, *162*, 837–840. [CrossRef]

23. Eiringhaus, J.; Zormpas, C.; Hohmann, S.; Mueller-Leisse, J.; Hillmann, H.A.; Duncker, D.; Veltmann, C. Premature end of service of implantable cardioverter-defibrillator by magnetic interference with left-ventricular assist device. *Hear. Case Rep.* **2021**, *7*, 691–693. [CrossRef] [PubMed]

24. Baliga, B.J. Chapter 13—IGBT Applications: Medical. In *The IGBT Device*; Baliga, B.J., Ed.; William Andrew Publishing: Amsterdam, The Netherlands, 2015; pp. 405–450.